Particle & Particle Systems Characterization

Particle & Particle Systems Characterization
www.particle-journal.com

RESEARCH ARTICLE

Highly Uniform SERS Substrates Based on Ligand Concentration-Gradient Modulated Gold Nanobipyramid Self-Assembled Monolayers

Kun-Peng Wang[1] | Jie Liu[1] | Xiaoyu Zhao[2] | Zhigang Zhou[1] | Tian-Song Deng[1]

[1]School of Electronics and Information Engineering, Hangzhou Dianzi University, Hangzhou, P. R. China | [2]College of Materials and Environmental Engineering, Hangzhou Dianzi University, Hangzhou, P. R. China

Correspondence: Jie Liu (liujie4209@hdu.edu.cn) | Tian-Song Deng (dengts@pku.edu.cn)

Received: 18 March 2026 | **Revised:** 16 May 2026 | **Accepted:** 11 June 2026

Keywords: gold nanobipyramids | localized surface plasmon resonance | self-assembled monolayer | SERS | thiol-terminated polystyrene

ABSTRACT

Controlling the tip arrangement and interparticle gaps in gold nanobipyramids (AuNBPs) self-assembled monolayers remains a critical challenge for achieving uniform surface-enhanced Raman scattering (SERS) hotspots. Herein, we demonstrate a facile liquid–gas interface self-assembly strategy modulated by a free ligand concentration gradient to precisely engineer tip-overlapping structures. By tuning the concentration of free thiol-terminated polystyrene (PS-SH) ligands (0–1.2 mg/mL), we achieve a continuous evolution of AuNBPs tip arrangements—from separated gaps (~6 nm) to tip alignment, and further to tunable tip-overlapping configurations (overlap length up to 18 nm). Combined experimental and finite-difference time-domain (FDTD) simulations reveal that the tip-overlapping structure formed at 1.2 mg/mL induces strong electromagnetic coupling, generating dense and uniform hotspots. Consequently, the optimized substrate exhibits exceptional SERS performance for crystal violet detection, with a wide linear range (10^{-3}–10^{-7} M, R^2 = 0.968), and outstanding signal uniformity (RSD = 3.78%). Conversely, excess ligands (>1.2 mg/mL) trigger entropy-driven three-dimensional disorder, degrading performance. This work provides a practical strategy for designing sensitive and reproducible SERS substrates through nanoscale structural engineering, while also highlighting the importance of balancing hotspot optimization and ligand-mediated molecular accessibility.

1 | Introduction

SERS as an ultrahigh-sensitivity detection technique [1–4] in molecular spectroscopy analysis [5, 6], holds an irreplaceable position in fields such as chemical analysis [7], biosensing [8, 9], environmental monitoring [10, 11], and rapid food safety screening [12, 13] due to its capabilities for single-molecule level detection, molecular-specific recognition, and non-destructive testing [14]. Its enhancement mechanisms originate from the localized surface plasmon resonance (LSPR) effect of noble metal nanostructures (e.g., gold and silver nanoparticles) and the "hotspots" effect excited within nanogaps [15–18]. However, conventional SERS substrate preparation methods predominantly rely on the random aggregation of nanoparticles or complex chemical modification processes, leading to insufficient signal reproducibility (relative standard deviation typically exceeding 10%), difficulties in quantitative analysis, and challenges in achieving large-area uniformity control. These limitations significantly hinder their practical application and widespread adoption [19, 20].

In recent years, the controlled self-assembly technology of noble metal nanoparticles has emerged as a core approach for enhancing SERS substrate performance due to its ability

to precisely regulate the spatial arrangement and interactions of nanostructures [21]. For instance, Zhang et al. transferred gold nanorods from aqueous solution into non-polar solvents, enabling their modification with 3-mercaptopropyl trimethoxysilane and octadecyltrimethoxysilane. The modified particles could be stably dispersed in toluene and formed self-assembled films at the air-water interface via self-assembly [22]. Zhou et al. demonstrated a manipulable method for preparing monolayer structures composed of gold rough nanocubes derived from gold nanocubes. This structure exhibited efficient and reproducible SERS activity for detecting organic pollutants and pesticide residues [23]. However, neither gold nanorods nor gold nanocubes exhibit enhancement effects as potent as AuNBPs. The significantly enhanced LSPR effect generated at the tips of AuNBPs renders them highly promising for SERS substrate construction [24]. Currently, the controllable synthesis of AuNBPs self-assembled monolayers faces dual challenges. On one hand, conventional close-packing or random adsorption methods struggle to effectively suppress non-specific particle aggregation, leading to increased substrate surface defects [25, 26]. For example, Li et al. found that gold nanoparticle arrays assembled at a three-phase liquid-liquid interface could undergo further contraction of nanogaps via electrostatic interactions upon immersion in halogen ion solutions, forming large-scale, tightly packed nanoparticle arrays with an average adjacent particle gap of less than 3 nm [27]. Li et al. also assembled low-symmetry Kagome superlattices using DNA-modified AuNBPs. By tuning the bipyramid size and DNA length, they constructed two types of superlattices with rhombohedral unit cells; one featured periodically stacked Kagome lattices showing characteristics like lattice distortion, bipyramid twisting, and planar chirality [28]. Both approaches exhibited issues with self-assembly defects. On the other hand, residual surface ligands (e.g., thiolated benzoic acid) often require complex post-treatment steps (e.g., acid washing, solvent extraction), which not only increase process costs but can also damage the LSPR properties of the particle surfaces [29, 30]. For instance, Shi et al. reported a two-dimensional nanoparticle liquid crystal superstructure self-assembled from AuNBPs, exhibiting four distinct orientational arrangements: horizontal (H-NLCS), circular (C-NLCS), slanted (S-NLCS), and vertical (V-NLCS). Among these, V-NLCS demonstrated the highest Raman enhancement factor, approximately 77 times higher than H-NLCS and about 19 times higher than C-NLCS [31]. Ding et al. proposed a novel strategy to enhance SERS performance by precisely controlling tip arrangements of AuNBPs within two-dimensional (2D) superlattices [32]. This method involved ligand exchange of the AuNBPs followed by regulating the amount of free ligands during liquid-gas interface self-assembly, successfully fabricating large-area, transferable superlattice films with various configurations [33–35].

However, despite significant progress in plasmonic nanostructure assembly, several critical challenges remain unresolved for practical SERS applications. Conventional self-assembly methods often suffer from poor signal reproducibility (relative standard deviation typically exceeding 10%), non-uniform hotspot distribution, and difficulties in achieving large-area uniformity control, which significantly hinder their quantitative analysis and widespread adoption. To address the challenge of controllable synthesis for AuNBPs self-assembled films, this study proposes an optimized liquid-gas interface self-assembly strategy combined with the dynamic modulation of free-state ligands. This approach aims to achieve precise control over the tip arrangement mode and gap size of AuNBPs, to explore their influence on SERS performance, and to improve the local signal uniformity of AuNBPs-based SERS substrates within ordered monolayer regions. Furthermore, we tested the SERS performance of self-assembled films formed from AuNBPs with different amounts of added free-state ligands. CV was employed as the probe dye throughout our experiments. By measuring the Raman signal intensity of CV, we observed that the Raman signal initially increased and then decreased with increasing concentrations of free-state ligands. To substantiate our findings, we performed finite-difference time-domain (FDTD) simulations. The simulation results demonstrated that as the tip gap between adjacent AuNBPs decreased, the surrounding electric field strength progressively intensified, and the number of SERS hotspots gradually increased, showing good agreement with our experimental observations.

2 | Results and Discussion

2.1 | Synthesis, Purification, and Modification of AuNBPs

In this study, purified AuNBPs underwent surface modification to construct self-assembled monolayers with SERS effects via liquid-gas interface self-assembly. The specific procedure is illustrated in Figure 1: Figure 1a depicts the experimental process of monolayer formation, where PS-SH-modified AuNBPs concentrated in toluene were drop-cast onto an ethylene glycol (EG) surface. Upon slow evaporation of toluene, the AuNBPs spontaneously assembled into a well-ordered, densely packed monolayer. Figure 1b shows a schematic of the ligand exchange process on AuNBPs surfaces, where CTAB was replaced by PS-SH during modification. Figure 1c presents a transmission electron microscopy (TEM) image of purified AuNBPs. Statistical analysis of approximately 150 AuNBPs revealed an average length of 80.7 ± 3.3 nm, an average diameter of 27.0 ± 0.9 nm, and an aspect ratio of approximately 3.0.

Figure S1 displays extinction spectra and photographic images of AuNBPs before and after purification and modification. In Figure S1a, the black spectrum corresponds to the initially synthesized AuNBPs via the seed-mediated growth method, exhibiting a longitudinal plasmon peak at 811 nm with a full width at half maximum (FWHM) of 65 nm. The red spectrum represents purified AuNBPs, showing a blue-shifted longitudinal peak at 797 nm with a reduced FWHM of 57 nm. Comparative analysis of normalized spectra further indicated a significant decrease in the intensity of the lateral plasmon peak around 500 nm after purification. These results collectively demonstrate high purity (>90%) of the purified AuNBPs, as confirmed by TEM statistical analysis. The blue spectrum corresponds to PS-SH-modified AuNBPs, with the longitudinal peak remaining nearly unchanged at 810 nm, indicating stable dispersion in toluene without aggregation.

To verify successful replacement of CTAB by PS-SH, PS-SH-modified AuNBPs dispersed in toluene were mixed with water. Figure S1b contrasts AuNBPs-CTAB aqueous solution (left vial: toluene upper phase, AuNBPs-CTAB aqueous lower phase)

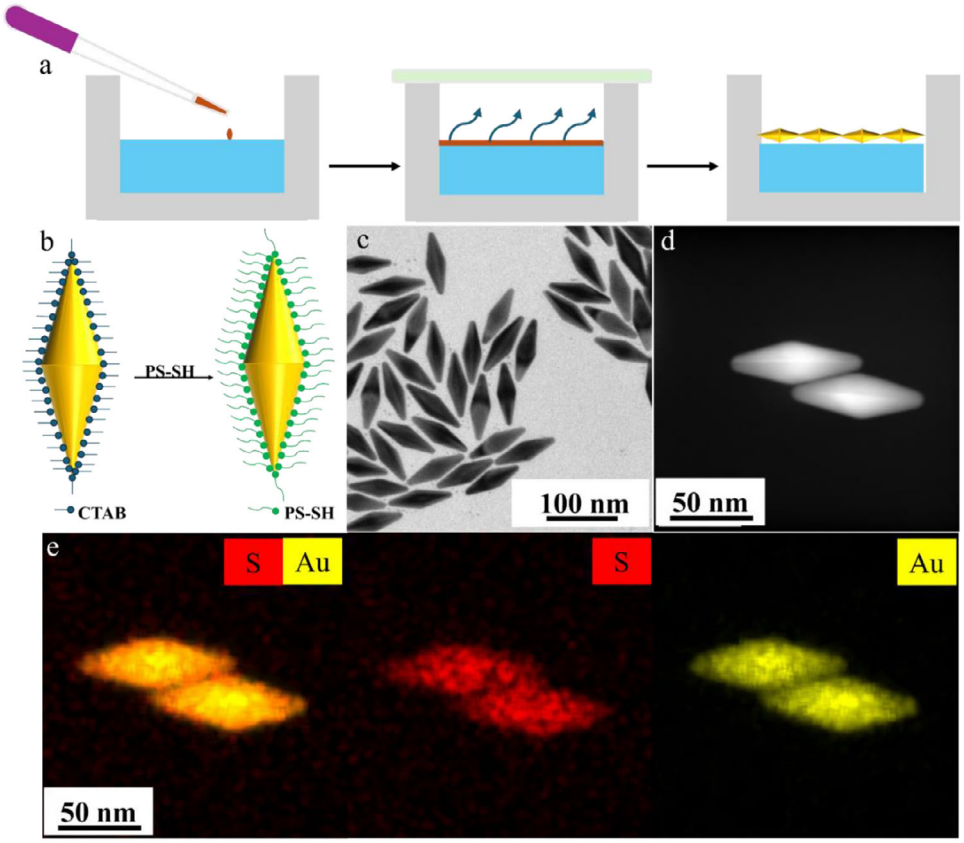

FIGURE 1 | Synthesis and self-assembly of AuNBPs. (a) Schematic illustration of the liquid-gas interface self-assembly process for AuNBPs. (b) Schematic illustration of the ligand exchange process for AuNBPs. (c) Transmission electron microscopy (TEM) image of AuNBPs. (d) High-angle annular dark-field scanning transmission electron microscopy (HAADF-STEM) image. (e) EDS mapping of PS-SH modified AuNBPs.

and AuNBPs-PS-SH toluene solution (right vial: AuNBPs-PS-SH toluene upper phase, water lower phase). The pronounced phase separation phenomenon confirms successful ligand modification that converted AuNBPs from hydrophilic to oleophilic.

Further evidence of successful PS-SH modification was provided by high-angle annular dark-field scanning transmission electron microscopy (HAADF-STEM) imaging (Figure 1d) and energy-dispersive X-ray spectroscopy (EDS) elemental mapping (Figure 1e). As PS-SH modified AuNBPs contain sulfur atoms, the distinct spatial distributions of gold and sulfur elements in the mapping results unequivocally demonstrate successful PS-SH functionalization on the AuNBPs surfaces.

2.2 | Self-Assembled Monolayer

We employed liquid-gas interface self-assembly to form monolayers. Figure S2 displays a photograph and a low-magnification scanning electron microscopy (SEM) image of a monolayer self-assembled from AuNBPs-PS-SH. The photograph reveals that the self-assembled monolayer spans approximately 1×1 cm^2 and exhibits a distinctly bright, uniform golden-yellow color, contrasting markedly with the brown hue of the AuNBPs solution. This color change indicates highly ordered interparticle arrangement within the monolayer, a pattern further corroborated by the low-magnification SEM image. Further investigation focused on modulating the interparticle spacing within the self-assembled monolayers. We demonstrated that varying the concentration of added free PS-SH substantially modulates the spacing between AuNBPs particles in the monolayer. In our experiments, 20 μL of AuNBPs-PS-SH solution was combined with 10 μL of PS-SH solution at different concentrations (all in toluene), totaling 30 μL. This mixture was drop-casted onto an ethylene glycol (EG) surface and covered with a glass slide to facilitate slow toluene evaporation. Figure 2a–d present transmission electron microscopy (TEM) images of monolayers formed with increasing free PS-SH concentrations (0-1.2 mg/mL).

TEM imaging reveals that the monolayers consist of densely packed rows of AuNBPs aligned along their longitudinal axes, with these rows arranged in a highly ordered parallel configuration to form the monolayer. Without added free PS-SH (Figure 2a), significant gaps exist between adjacent AuNBPs within the same row, with an average measured gap of 6.1 ± 0.3 nm. As the free PS-SH concentration increased, adjacent AuNBPs within the same row progressively moved closer, exhibiting a tip overlapping appearance in the two-dimensional projection. At 0.4 mg/mL free PS-SH (Figure 2b), adjacent particles predominantly achieved tip-to-tip alignment (exhibiting a mixture of small gaps and incipient overlap, average tip gap 0.8 ± 1.1 nm). At 0.8 mg/mL (Figure 2c), all adjacent AuNBPs within rows demonstrated clear tip overlap, with an average overlapping length of 7.9 ± 0.8 nm. Further increasing the concentration to 1.2 mg/mL (Figure 2d) resulted in significantly enhanced tip overlap, reaching an average overlapping length of

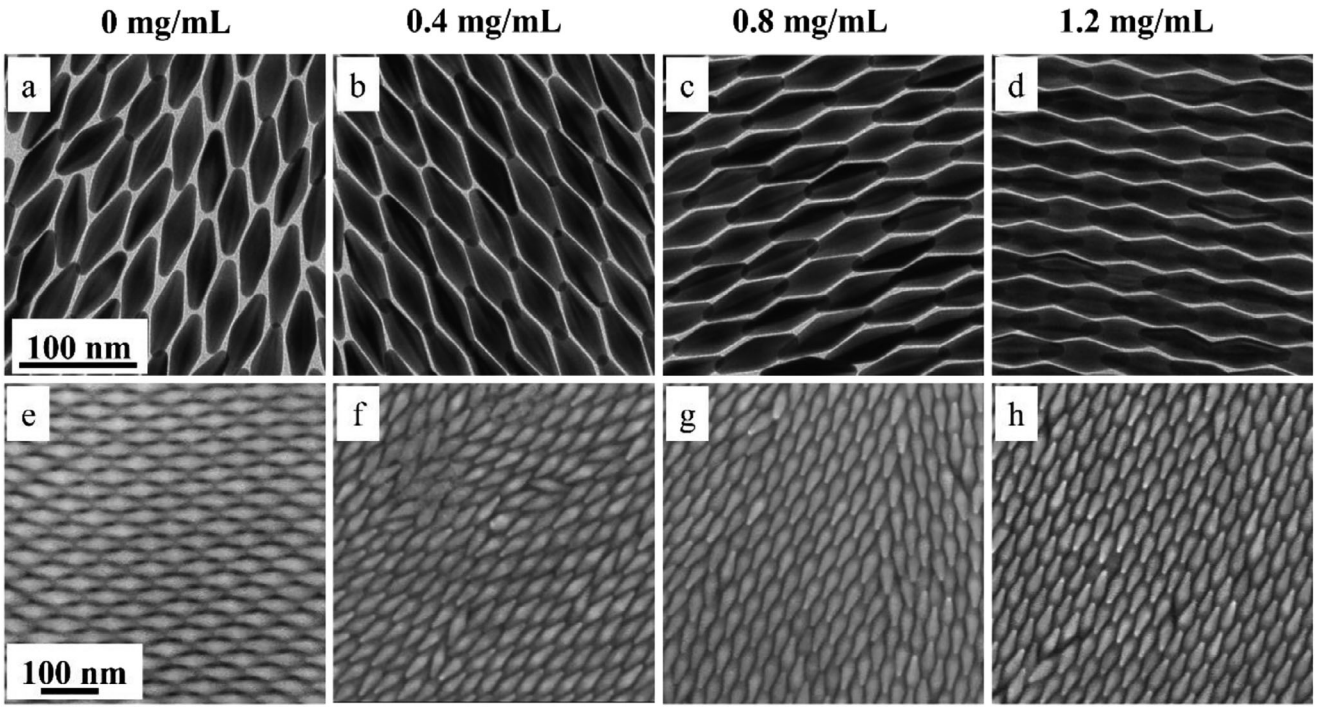

FIGURE 2 | Characterization of the monolayer structure self-assembled from AuNBPs-PS-SH. (a-d) TEM images of self-assembled monolayers formed with different concentrations of free PS-SH. (e-h) Corresponding scanning electron microscopy (SEM) images.

18.2 ± 1.5 nm. Crucially, the inter-row spacing remained largely unchanged across this concentration range.

A distinct structural transition occurred at higher free PS-SH concentrations. Figure S3a shows the TEM image of the structure formed with 2 mg/mL free PS-SH. Here, the AuNBPs lost their parallel row alignment and adopted a disordered arrangement with significantly increased spacing (average particle spacing: length 16.2 ± 1.7 nm, width 8.1 ± 1.3 nm). Figure S3b reveals that at 4 mg/mL free PS-SH, disordered multilayered aggregates formed instead of a monolayer. These observations establish the principle: precisely modulating free PS-SH concentration (0–1.2 mg/mL) allows accurate control over intra-row particle spacing within AuNBPs monolayers. Increasing concentration substantially enhances interparticle attraction, driving the transition within a row from separated gaps (6.1 ± 0.3 nm at 0 mg/mL) to progressively increasing tip overlap (up to 18.2 ± 1.5 nm at 1.2 mg/mL). This tunability arises from the dynamic PS-SH ligand layer formed at the AuNBPs tips: its desolvation effects and chain entanglement overcome steric hindrance, drawing particles together [36]. However, exceeding the critical threshold (>1.2 mg/mL) induces entropy-dominated interparticle repulsion, leading to three-dimensional disordered aggregation and ultimately, collapse of the monolayer architecture. Figure 2e–h show corresponding high-magnification SEM images for free PS-SH concentrations from 0 to 1.2 mg/mL. These images exhibit the same concentration-dependent spacing and tip arrangement trends observed via TEM. Crucially, the SEM images provide clear visual confirmation that the tip overlapping structure arises from a "tip-on-tip" configuration, where the tip of one AuNBPs physically rests upon the tip of its neighbor.

2.3 | SERS Performance of Self-Assembled Monolayers

The SERS performance of AuNBPs monolayers was evaluated by detecting CV (10^{-5} M). Figure 3a shows the Raman spectra of CV (10^{-5} M) adsorbed on self-assembled monolayers formed with varying concentrations of free PS-SH. A clear trend emerges: Raman intensity progressively increases from 0 to 1.2 mg/mL free PS-SH, peaks at 1.2 mg/mL, and subsequently diminishes when concentration further increases to 4 mg/mL. This concentration-dependent enhancement is more quantitatively evident in Figure 3b, which compares the Raman intensities at 1172 cm^{-1} extracted from the spectra in Figure 3a. Figure 3c displays the Raman spectra of CV, Rhodamine 6G (R6G), and Methylene Blue (MB), both individually and as a mixture. All dye molecules were detected on AuNBPs monolayers self-assembled with 1.2 mg/mL free PS-SH, which corresponds to the optimized tip-overlapping configuration exhibiting the strongest electromagnetic coupling and highest SERS enhancement. Characteristic peaks of all dye molecules remain identifiable in both pure and mixed states, indicating that the optimized AuNBPs monolayer can distinguish several representative Raman-active dye molecules. It should be noted that the spectra of CV, R6G, MB, and their mixture were acquired under identical Raman acquisition parameters. The higher signal-to-noise ratio and sharper peak definition observed for R6G may arise from its larger Raman scattering cross-section, favorable molecular orientation, and stronger effective adsorption or retention within the PS-SH-modified plasmonic environment. Therefore, the present results demonstrate multi-dye distinguishability for selected dye probes rather than universal detection capability for all analytes.

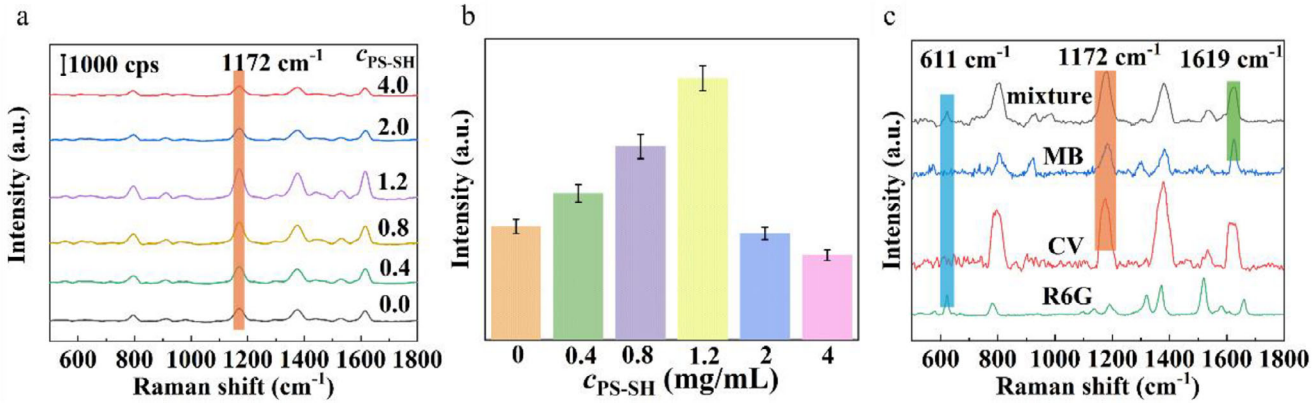

FIGURE 3 | (a) Raman spectra of Crystal Violet (CV, 10^{-5} M) adsorbed on self-assembled monolayers formed with varying concentrations of free PS-SH. (b) Comparison of Raman intensities at 1172 cm^{-1} for CV measured on different monolayer substrates. (c) Raman spectra of three dye molecules and their mixture.

The intrinsic Raman contribution from the PS-SH ligand layer is not obvious in the dye-loaded SERS spectra. This is reasonable because the Raman cross-sections of the dye molecules under 633 nm excitation are much larger than that of the polystyrene ligand, particularly for strongly Raman-active dyes such as CV, R6G, and MB. As a result, possible weak vibrational features from PS-SH, including phenyl-related modes or C–S vibrations, can be overwhelmed by the dye signals. In addition, only the polymer segments very close to the AuNBPs surface are located within the strongest electromagnetic enhancement region, whereas most PS chains extend away from the hotspot region. The brush-like conformation of the ligand layer may further weaken well-resolved ligand-related spectral features. Therefore, the spectral assignments in this work mainly focus on the characteristic Raman bands of the probe molecules. These results collectively indicate that the interparticle electromagnetic (EM) coupling within AuNBPs monolayers—tunable by the concentration of free PS-SH—significantly influences SERS enhancement. Nevertheless, the PS-SH ligand layer also introduces an inherent limitation. Although it is essential for controlling the liquid–air interfacial assembly and regulating the tip arrangement of AuNBPs, the ligand layer partially passivates the gold surface and may hinder the diffusion or adsorption of analytes with weak affinity toward either gold or the polystyrene environment. Therefore, the present substrate is expected to be more suitable for molecules that can be effectively retained near the ligand-modified hotspot region. For analytes with low surface affinity, further surface engineering, such as optimizing ligand density, introducing analyte-enrichment layers, or designing partially accessible hotspot interfaces, may be required. The demonstrated capability for selected multi-dye identification underscores the substantial potential of these substrates for practical sensing applications.

Figure 4a presents the Raman mapping corresponding to the 1172 cm^{-1} peak for CV (10^{-5} M) adsorbed on the AuNBPs monolayer formed with 1.2 mg/mL PS-SH. A representative 10 μm × 10 μm square area was scanned across 100 distinct points, providing compelling evidence for the excellent SERS uniformity within the selected ordered monolayer region. Figure 4b shows the Raman spectra of CV acquired at 20 randomly selected positions on the monolayer. The spectra exhibit remarkable consistency. Statistical analysis of the Raman intensities at 1172 cm^{-1} yielded a relative standard deviation (RSD) as low as 3.78% (Figure 4c), confirming excellent local signal reproducibility within the selected ordered monolayer region. It should be emphasized that this RSD value represents the intra-area uniformity at the micrometer scale rather than the absolute uniformity over the entire centimeter-scale transferred film. As suggested by the optical image and low-magnification SEM image in Figure S2, minor macroscopic defects and local discontinuities can still exist after liquid–air interfacial assembly and film transfer. Therefore, inter-region or inter-sample variations may be larger than the local RSD value reported here. The high reproducibility demonstrated in this work mainly arises from the ordered AuNBPs packing and uniform hotspot distribution within locally continuous monolayer domains.

To investigate the relationship between the concentration of CV deposited on the AuNBPs monolayer and the corresponding SERS intensity, solutions of CV with varying concentrations (10^{-3} M to 10^{-7} M) were drop-casted onto monolayers prepared using 1.2 mg/mL PS-SH. Figure 4d displays the concentration-dependent Raman spectra. A clear trend emerges: the SERS intensity progressively increases with higher concentrations of CV. The prominent peak at 1172 cm^{-1} is primarily attributed to the in-plane C-C stretching vibration of the benzene ring backbone. This assignment represents the core and most reliable vibrational mode for this dye molecule at this wavenumber. The plot in Figure 4e illustrates the linear correlation between the Raman intensity at 1172 cm^{-1} and the CV concentration across the range of 10^{-3} M to 10^{-7} M, yielding a coefficient of determination (R^2) of 0.96802. This demonstrates the excellent SERS sensitivity of the substrate. These results indicate that the AuNBPs monolayer is capable of sensitive detection for practical samples, demonstrating considerable potential for diverse sensing applications.

2.4 | Finite-Difference Time-Domain (FDTD) Simulations

To validate the experimental findings, we performed finite-difference time-domain (FDTD) simulations to model the

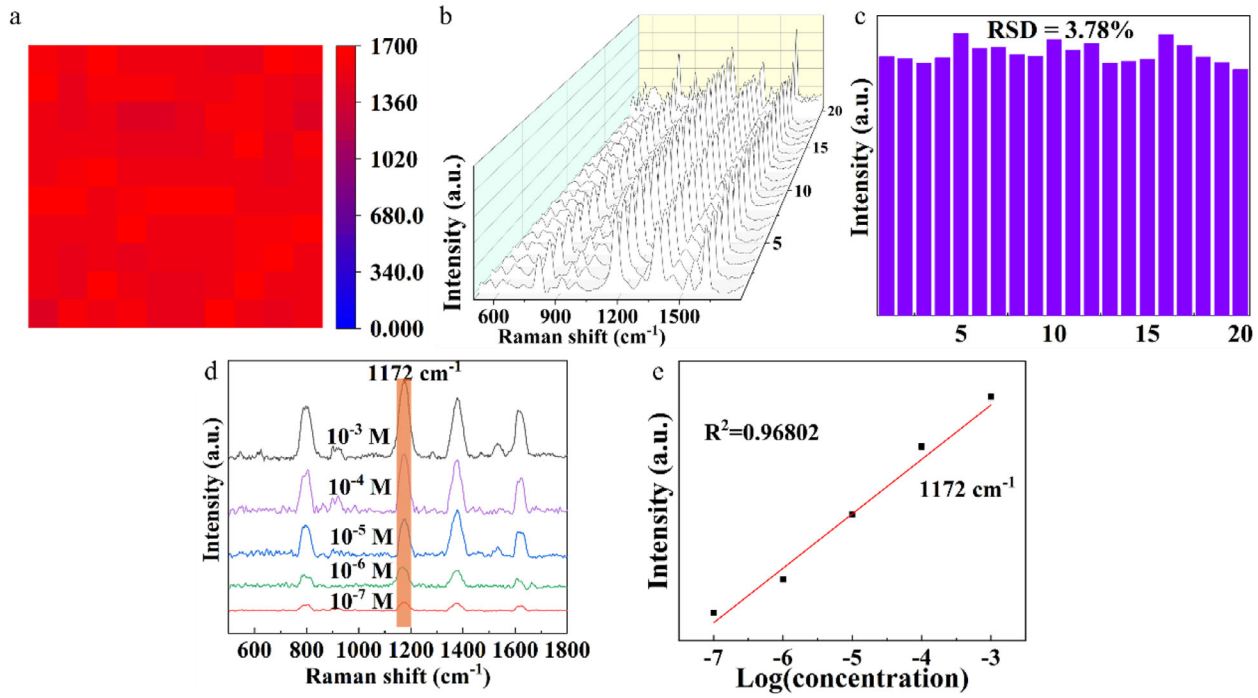

FIGURE 4 | (a) Raman mapping corresponding to the 1172 cm^{-1} peak for CV (10^{-5} M) adsorbed on the AuNBPs monolayer formed with 1.2 mg/mL PS-SH. (b) Raman spectra of CV measured at 20 different spots within the selected ordered monolayer region and (c) their intensities at 1172 cm^{-1}. (d) Concentration-dependent Raman spectra and (e) plots of SERS intensity vs. concentration for crystal violet collected on the optimized AuNBPs monolayer.

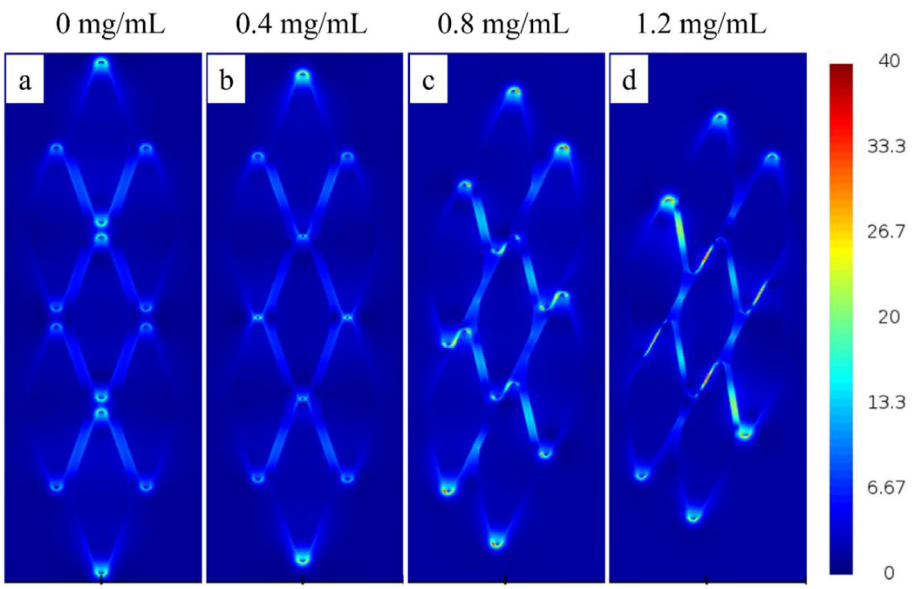

FIGURE 5 | FDTD simulations of electric field intensity distributions for AuNBPs monolayers self-assembled with varying concentrations of free PS-SH ligands (a) 0 mg/mL, (b) 0.4 mg/mL, (c) 0.8 mg/mL, and (d) 1.2 mg/mL.

electromagnetic field distribution of the AuNBPs monolayers. Computational models were constructed based on the TEM and SEM images of self-assembled monolayers in Figure 2. The dimensions of the AuNBPs particles precisely matched those of the synthesized AuNBPs, as depicted in Figure 5. Simulations utilized a 633 nm excitation wavelength to align with experimental conditions, with incident light polarized parallel to the longitudinal axis of the AuNBPs.

This polarization configuration was selected to evaluate the strongest longitudinal plasmon coupling between adjacent AuNBPs. In the Raman measurements, the sample was tested

in the standard backscattering configuration of the Raman microscope without actively rotating the substrate to align the AuNBPs rows with the incident laser polarization. Therefore, the experimentally measured SERS signals should be regarded as an orientation-averaged response from local AuNBPs domains within the laser spot. Because the longitudinal plasmon mode of AuNBPs is polarization-sensitive, local variations in the in-plane orientation of AuNBPs rows may contribute to spot-to-spot intensity fluctuations. Accordingly, the FDTD results represent the optimized coupling configuration and provide mechanistic insight into the trend of hotspot enhancement, rather than a complete description of all possible in-plane orientations in the experimental monolayer.

Figure 5 shows the simulated electric field intensity distributions for AuNBPs monolayers self-assembled with different concentrations of free PS-SH. A clear trend emerges: the electric field intensity progressively strengthened with increasing free PS-SH concentration, reaching its maximum at 1.2 mg/mL. Specifically, at 0 mg/mL (Figure 5a), the field intensity is relatively low, with a maximum value of approximately 12 localized at the tips. As the concentration increases to 0.4 mg/mL (Figure 5b), the intensity rises to ∼15 due to reduced interparticle gaps. At 0.8 mg/mL (Figure 5c), significant enhancement is observed as tip overlapping initiates, yielding a field intensity of ∼23. The maximum enhancement is achieved at 1.2 mg/mL (Figure 5d), where the tight tip-overlapping configuration drives the electric field intensity to a peak value of ∼38. For all AuNBPs monolayers, intense and concentrated electromagnetic fields are generated within the nanogaps between particles. This enhancement is attributed to the dense array of gaps and crevices formed among the gold nanoparticles within the monolayer, coupled with progressively reduced interparticle distances, which dramatically intensified particle-particle plasmonic coupling. These simulations reveal that strong electromagnetic coupling, along with dense and uniform hotspots, underpins the superior SERS performance. Simulations were extended to configurations formed with 2 mg/mL and 4 mg/mL free PS-SH (Figure S4). The resulting electric field intensity significantly weakened, aligning perfectly with experimental observations. At 2 mg/mL (Figure S4a), the intensity drops back to ∼12, and at 4 mg/mL (Figure S4b), it further decays to ∼8 due to structural disorder. Both computational and experimental results consistently confirm that the monolayer self-assembled with 1.2 mg/mL free PS-SH delivers optimal SERS enhancement.

3 | Conclusions

In summary, we have successfully developed a novel approach for precise tuning of tip gaps in AuNBPs self-assembled monolayers via a free ligand concentration gradient. Our study revealed that increasing the concentration of free PS-SH from 0 mg/mL to 1.2 mg/mL progressively drives the interparticle arrangement from separated gaps (6 nm) to tip-overlapping configurations (18 nm), substantially enhancing electromagnetic coupling. The tip-overlapping structure formed at 1.2 mg/mL yielded maximal SERS intensity for crystal violet detection and demonstrated excellent local signal uniformity within ordered monolayer regions, with an RSD of 3.78%. Furthermore, the AuNBPs monolayer substrate allowed the identification of characteristic Raman peaks from crystal violet, Rhodamine 6G, methylene blue, and their mixture, demonstrating its capability for selected multi-dye analysis. Nevertheless, because the AuNBPs surface is modified with a PS-SH ligand layer, analyte accessibility to plasmonic hotspots may depend strongly on molecular affinity toward the ligand-modified surface. Future optimization of ligand density and hotspot accessibility will be important for extending this platform to weakly adsorbing analytes and more complex practical samples. Furthermore, FDTD simulations confirmed that the overlapping geometry generates dense, uniform hotspots, while supra-threshold ligand concentrations induce hotspot deactivation through entropy-driven 3D disorder aggregation. This strategy overcomes the challenge of defect control in self-assembled monolayers and provides an engineerable solution for highly reproducible SERS detection in fields such as disease screening and environmental pollutant monitoring [37, 38].

4 | Experimental Section

4.1 | Materials

All chemicals were used as received without further purification. Hexadecyltrimethylammonium bromide (CTAB, >99.0%) was purchased from TCI America. Chloroauric acid ($HAuCl_4$), L-ascorbic acid (AA, >99.99%), hydrochloric acid (HCl, 37 wt.% in water), methyl blue, rhodamine 6G (R6G, 95%), crystal violet (90%), ethylene glycol (98%) and methanol (99.5%) were purchased from Shanghai Macklin Biochemical Technology Co., Ltd. Hexadecyltrimethylammonium chloride (CTAC, >99.0%), sodium borohydride (NaBH4, 98.0%), sodium citrate dihydrate (SC, 99.0%), silver nitrate ($AgNO_3$, >99.8%), benzyldimethylhexadecylammonium chloride (HDBAC 95.0%), and tetrahydrofuran (THF, 99.0%) were purchased from Shanghai Aladdin Biochemical Technology Co., Ltd. Thiol-terminated polystyrene (average Mn = 5000, PDI ≤ 1.1, named PS-SH-5 k) was purchased from Sigma-Aldrich. Toluene (TOL, ≥ 99.5%) was purchased from National Pharmaceutical Group Chemical Reagent Co., Ltd. Ultrapure water (>18.2 MΩ) obtained from a Milli-Q water system was used in all experiments. All glassware were cleaned using freshly prepared aqua regia (HCl in a 3:1 ratio by volume) followed by rinsing with copious amounts of water.

4.2 | Synthesis and Purification of AuNBPs

AuNBPs samples were prepared using a seed-mediated growth method [39]. Briefly, a freshly prepared ice-cold sodium borohydride solution (0.025 M, 0.25 mL) was rapidly added under vigorous stirring to a pre-mixed aqueous solution containing chloroauric acid ($HAuCl_4$, 0.01 M, 0.25 mL), sodium citrate dihydrate (SC, 0.01 M, 5.0 mL), and cetyltrimethylammonium chloride (CTAC, 0.1 M, 5.0 mL). After stirring for 2 min, the seed solution was transferred to an 80°C water bath and slowly stirred for 90 min, during which its color gradually changed from brown to red. The seed solution was then removed from the water bath and stored at room temperature. Next, 0.1 mL of the seed solution was added to the growth solution, which was composed of cetyltrimethylammonium bromide (CTAB, 0.1 M, 20.0 mL), chloroauric acid ($HAuCl_4$, 0.01 M, 1.0 mL), silver nitrate ($AgNO_3$, 0.01 M, 0.2 mL), hydrochloric acid (HCl, 1.0 M, 0.4 mL),

and L-ascorbic acid (AA, 0.1 M, 0.16 mL). The mixture was gently inverted and mixed for 10 s, then left undisturbed at 30°C overnight. To purify the AuNBPs, the solution was centrifuged at 8000 rpm for 10 min. After discarding the supernatant, the precipitate was redispersed in a CTAB solution (1.5 mM, 6.0 mL). Depletion flocculation was then applied to remove impurity particles by adding a high-concentration HDBAC solution (0.5 M, 14.0 mL), and the mixture was left undisturbed at 30°C in a water bath for 24 h. Subsequently, the purple supernatant was carefully decanted, and the precipitate was re-dispersed in a CTAB solution (1.5 mM, 5.0 mL), followed by ultrasonication for 1 min to disperse the precipitate. The resulting purified solution (brown) was centrifuged again at 8000 rpm for 10 min and washed twice with a CTAB solution (1.5 mM, 5.0 mL) to remove excess HDBAC. Finally, the purified AuNBPs were dispersed in a CTAB solution (1.5 mM, 1.0 mL) for subsequent experiments.

4.3 | Surface Modification of AuNBPs With Polystyrene Thiol (PS-SH)

An improved, simple, and efficient surface modification method was employed. First, 4 mg of PS-SH was dissolved in 2 mL of tetrahydrofuran (THF). Subsequently, the purified AuNBPs solution (1 mL) was centrifuged to remove the supernatant and then added to the THF solution. After ultrasonication for 120 min, the mixture was allowed to stand at room temperature for 24 h, during which PS-SH successfully replaced the original CTAB ligands on the AuNBPs surface, completing the surface modification. The solution was then centrifuged at 8000 rpm, and the supernatant was discarded. The precipitate was redispersed in 5 mL of methanol and centrifuged again for washing. Finally, 5 mL of toluene was added, and the solution was centrifuged and washed twice to remove excess PS-SH. The purified AuNBPs were dispersed in 0.15 mL of toluene and stored.

4.4 | Self-Assembly and Transfer of AuNBPs Monolayer

A liquid-air interfacial self-assembly method was employed to fabricate AuNBPs monolayer membranes [40]. First, 2 mL of ethylene glycol solution was added into the square wells of a polytetrafluoroethylene (Teflon) mold. Subsequently, 30 μL of PS-SH modified AuNBPs solution was carefully pipetted onto the ethylene glycol surface. The mold was then covered with a glass slide and placed in a 30°C environment, allowing toluene (solvent) to slowly evaporate through the gap between the Teflon mold and the glass slide. After 24 h, toluene completely evaporated to form a solid monolayer. For membrane transfer, a substrate was positioned beneath the floating membrane using tweezers and gently lifted upward to collect the membrane layer. Residual ethylene glycol was removed by drying the transferred membrane in a vacuum desiccator.

4.5 | SERS Performance Test

SERS measurements were conducted using a LabRAM HR Evolution Raman spectroscopy system with a 633 nm laser excitation source. Silicon wafers were used as substrates and were ultrasonically cleaned sequentially in acetone and ethanol, followed by drying. AuNBPs monolayer films were transferred onto the substrates via the method described above. Subsequently, 20 μL of a 10^{-5} M crystal violet (CV) solution was drop-cast onto the AuNBPs monolayer and allowed to dry prior to analysis. All spectra were acquired using a 100× objective lens, resulting in a laser spot size of approximately 1 μm, with a grating setting of 150 g/mm. Typical acquisition parameters included a laser power of 26 μW (attenuated by a 1% neutral density filter) and an integration time of 1 s. Unless otherwise stated, the Raman spectra of CV, rhodamine 6G (R6G), methylene blue (MB), and their mixtures were collected under identical experimental conditions.

4.6 | FDTD Simulations

The electric field in the monolayer film region was simulated using the FDTD Solutions software package (Lumerical Solutions Inc.). A total-field scattered-field (TFSF) source was used to simulate the interaction of a 633 nm plane wave with AuNBPs. The dimensions of the AuNBPs were set based on average experimental measured values, with mesh division of 1 nm within the boundaries. The spacing between AuNBPs was set according to the actual gap, and the refractive index of the surrounding medium was set to 1.4.

4.7 | Characterizations

All absorption measurements were captured on a UV-1900i spectrophotometer (SHIMADZU, Japan) with a 10-mm optical path, whereby a glass cuvette filled with Milli-Q water or toluene was used as the reference. Transmission electron microscopy (TEM) images were captured on a HT-7700 microscope (HITACHI, Japan) operating at 100.0 kV. Energy disperse spectroscopy (EDS) mapping was performed by a Fei-Talos-F200S operated at 200 kV. Scanning electron microscopy (SEM) images were captured using Sigma 500 operating at 3 kV. The SERS test was conducted using a LabRAM HR Evolution instrument with a laser wavelength of 633 nm and a laser power of 26 μW (attenuated by a 1% neutral density filter). The microscope images were captured using the built-in optical microscope of the Raman equipment with a 100 × objective lens.

Acknowledgements

The authors thank Sudan Shen for her assistance in TEM at State Key Laboratory of Chemical Engineering (Zhejiang University). The authors acknowledge financial support from Zhejiang Provincial Natural Science Foundation (Grant: LY24F050008), and National Natural Science Foundation of China (NSFC, Grant: 61905056). This work was also supported in part by Shanghai Industrial Collaborative Innovation Project under grant HCXBCY-2024-051.

Conflicts of Interest

The authors declare no conflict of interest.

Data Availability Statement

The data that support the findings of this study are available from the corresponding author upon reasonable request.

References

1. J. E. S. van der Hoeven, H. Gurunarayanan, M. Bransen, D. A. Matthijs de Winter, P. E. de Jongh, and A. Blaaderen, "Silica-Coated Gold Nanorod Supraparticles: A Tunable Platform for Surface Enhanced Raman Spectroscopy," *Advanced Functional Materials* 32 (2022): 2200148.

2. K. Xue, B. Lin, Q. Tang, et al., "Paper-Based 3D SERS Immunoassay Array Based on Self-Assembly of AuNBPs@Ag Nanorods for Ultrasensitive and Highly Stable Detection of α-Fetoprotein," *Microchemical Journal* 195 (2023): 109466, https://doi.org/10.1016/j.microc.2023.109466.

3. J. Yang, R. Zhang, J. Liu, et al., "Well-Ordered Au@Ag NBPs/SiO_2 Nanoarray for Sensitive Detection of Chloramphenicol via DNAzyme-Assisted SERS Sensing," *Food Chemistry* 454 (2024): 139806, https://doi.org/10.1016/j.foodchem.2024.139806.

4. M. Zhang, J. Liu, X. Li, X. Zhao, Z. Cheng, and T.-S. Deng, "Versatile Approach to Self-Assembly of Surface Modified Nanoparticles Into SERS-Active Nanoclusters," *Particle & Particle Systems Characterization* 41 (2024): 2400034, https://doi.org/10.1002/ppsc.202400034.

5. Y. Hirai and H. Yabu, "Self-Assembled Microrings of Au Nanoparticle and Au Nanorod Clusters Formed at the Equators of Janus Particles," *RSC Advances* 9 (2019): 17183–17186, https://doi.org/10.1039/C9RA02767J.

6. M. U. Amin and J. Fang, "Self-Assembled Gold Nano-Bipyramids for Solution-Based Surface-Enhanced Raman Spectroscopy Detection," *ACS Applied Nano Materials* 5 (2022): 10421–10430, https://doi.org/10.1021/acsanm.2c01779.

7. K. Chang, Y. Zhao, M. Wang, et al., "Advances in Metal-Organic Framework-Plasmonic Metal Composites Based SERS Platforms: Engineering Strategies in Chemical Sensing, Practical Applications and Future Perspectives in Food Safety," *Chemical Engineering Journal* 459 (2023): 141539, https://doi.org/10.1016/j.cej.2023.141539.

8. Q. Li, H. Huo, Y. Wu, et al., "Design and Synthesis of SERS Materials for in Vivo Molecular Imaging and Biosensing," *Advanced Science* 10 (2023): 2202051, https://doi.org/10.1002/advs.202202051.

9. C. Lin, Y. Li, Y. Peng, et al., "Recent Development of Surface-Enhanced Raman Scattering for Biosensing," *Journal of Nanobiotechnology* 21 (2023): 149, https://doi.org/10.1186/s12951-023-01890-7.

10. X. Li, X. Chen, J. Liu, et al., "Superparticles of Gold Nanorods With Controllable Bandwidth and Spectral Shape for Lipophilic SERS," *Nanoscale* 15 (2023): 12270–12279, https://doi.org/10.1039/D3NR01883K.

11. G.-L. Wu, T.-S. Deng, K.-P. Wang, et al., "Synthesis of Lipophilic Gold Nanorod Superparticles and Their Size-Dependent SERS Performances," *Journal of Nanoparticle Research* 27 (2025): 19, https://doi.org/10.1007/s11051-025-06216-2.

12. X. Huang, B. Sheng, H. Tian, et al., "Real-Time SERS Monitoring Anticancer Drug Release along with SERS/MR Imaging for PH- Sensitive Chemo-Phototherapy," *Acta Pharmaceutica Sinica B* 13 (2023): 1303–1317, https://doi.org/10.1016/j.apsb.2022.08.024.

13. T. Itoh, M. Procházka, Z.-C. Dong, et al., "Toward a New Era of SERS and TERS at the Nanometer Scale: From Fundamentals to Innovative Application," *Chemical Reviews* 123 (2023): 1552–1634, https://doi.org/10.1021/acs.chemrev.2c00316.

14. Y. Wang, J. Chen, Y. Zhong, S. Jeong, R. Li, and X. Ye, "Structural Diversity in Dimension-Controlled Assemblies of Tetrahedral Gold Nanocrystals," *Journal of the American Chemical Society* 144 (2022): 13538–13546, https://doi.org/10.1021/jacs.2c03196.

15. L. Zhang, Y. Yu, X. Zhu, et al., "Tailorable Janus Plasmonic SERS Platform With Hotspots Integrating and Analytes Enriching Property for Multiple Sensing," *Sensors and Actuators B: Chemical* 413 (2024): 135721, https://doi.org/10.1016/j.snb.2024.135721.

16. H. Yabu, S. Yokokura, and S. Shimizu, "Gold Nanoparticle-Decorated Polymer Particles for High-Optical-Density Immunoassay Probes," *Langmuir* 40 (2024): 3268–3273, https://doi.org/10.1021/acs.langmuir.3c03890.

17. S. Wan, X. Xia, Y. Gao, et al., "Curvature-Guided Depletion Stabilizes Kagome Superlattices of Nanocrystals," *Science* 387 (2025): 978–984, https://doi.org/10.1126/science.adu4125.

18. Y. Liu, K. K. Chui, Y. Fang, S. Wen, X. Zhuo, and J. Wang, "Metal–Organic Framework-Enabled Trapping of Volatile Organic Compounds Into Plasmonic Nanogaps for Surface-Enhanced Raman Scattering Detection," *ACS Nano* 18 (2024): 11234–11244, https://doi.org/10.1021/acsnano.4c00208.

19. M. Shao, C. Ji, J. Tan, et al., "Ferroelectrically Modulate the Fermi Level of Graphene Oxide to Enhance SERS Response," *Opto-Electronic Advances* 6 (2023): 230094, https://doi.org/10.29026/oea.2023.230094.

20. Y. Zhang, Z. Yang, Y. Zou, S. Farooq, Y. Li, and H. Zhang, "Novel Ag-Coated Nanofibers Prepared by Electrospraying as a SERS Platform for Ultrasensitive and Selective Detection of Nitrite in Food," *Food Chemistry* 412 (2023): 135563, https://doi.org/10.1016/j.foodchem.2023.135563.

21. C. Chen, Y. Zhang, X. Wang, X. Qiao, G. I. N. Waterhouse, and Z. Xu, "A Core-Satellite Self-Assembled SERS Aptasensor Containing A "Biological-Silent Region" Raman Tag for the Accurate and Ultrasensitive Detection of Histamine," *Food Science and Human Wellness* 13 (2024): 1029–1039, https://doi.org/10.26599/FSHW.2022.9250089.

22. M. Zhang, T.-S. Deng, and Z. Cheng, "Ethanol as a 'Catalyst' for Effective Phase Transfer and Self-Assembly of Gold Nanorods," *Chemistryselect* 8 (2023): 202301065, https://doi.org/10.1002/slct.202301065.

23. Z.-R. Zhou, W.-X. Liu, Z.-Y. Yao, et al., "Uniform and Dense Hotspots in Au Rough-Nanocube Monolayer for Sensitive and Reproducible SERS Detection," *ACS Applied Nano Materials* 7 (2024): 17009–17016, https://doi.org/10.1021/acsanm.4c03144.

24. H. Cheng, R. Chen, Y. Zhan, et al., "Novel Ratiometric Surface-Enhanced Raman Scattering (SERS) Biosensor for Ultrasensitive Quantitative Monitoring of Human Carboxylesterase-1 in Hepatocellular Carcinoma Cells Using Ag–Au Nanoflowers as SERS Substrate," *Analytical Chemistry* 96 (2024): 18555–18563, https://doi.org/10.1021/acs.analchem.4c04763.

25. L. Liu, Y. Wang, Z. Xue, B. Peng, X. Kou, and Z. Gao, "Research Progress of Dual-Mode Sensing Technology Strategy Based on SERS and Its Application in the Detection of Harmful Substances in Foods," *Trends in Food Science & Technology* 148 (2024): 104487.

26. Y. Liu, M. Li, H. Liu, C. Kang, and C. Wang, "Cancer Diagnosis Using Label-Free SERS-Based Exosome Analysis," *Theranostics* 14 (2024): 1966–1981, https://doi.org/10.7150/thno.92621.

27. X. Li, D. Zhang, L. Wang, et al., "Shrinking Gap between Nanoparticles in Gold Nanofilms to Enhance Surface-Enhanced Raman Spectroscopy Performance Investigated by both Experimental and Theoretical Methods," *Applied Surface Science* 638 (2023): 157823, https://doi.org/10.1016/j.apsusc.2023.157823.

28. Z. Li, Y. Lim, I. Tanriover, et al., "DNA-Mediated Assembly of Au Bipyramids Into Anisotropic Light Emitting Kagome Superlattices," *Science Advances* 10 (2024): adp3756, https://doi.org/10.1126/sciadv.adp3756.

29. H. Ma, S.-Q. Pan, W.-L. Wang, et al., "Surface-Enhanced Raman Spectroscopy: Current Understanding, Challenges, and Opportunities," *ACS Nano* 18 (2024): 14000.

30. S. M. Sibug-Torres, D.-B. Grys, G. Kang, et al., "In Situ Electrochemical Regeneration of Nanogap Hotspots for Continuously Reusable Ultrathin SERS Sensors," *Nature Communications* 15 (2024): 2022.

31. Q. Shi, K. J. Si, D. Sikdar, L. W. Yap, M. Premaratne, and W. Cheng, "Two-Dimensional Bipyramid Plasmonic Nanoparticle Liquid Crystalline Superstructure With Four Distinct Orientational Packing Orders," *ACS Nano* 10 (2016): 967–976, https://doi.org/10.1021/acsnano.5b06206.

32. W. Ding, Y. Xia, H. Song, T. Li, D. Yang, and A. Dong, "Macroscopic Superlattice Membranes Self-Assembled From Gold Nanobipyramids With Precisely Tunable Tip Arrangements for SERS," *Angewandte Chemie International Edition* 63 (2024): 202401945, https://doi.org/10.1002/anie.202401945.

33. X. Tang, Q. Hao, X. Hou, et al., "Exploring and Engineering 2D Transition Metal Dichalcogenides Toward Ultimate SERS Performance," *Advanced Materials* 36 (2024): 2312348, https://doi.org/10.1002/adma.202312348.

34. Q. Wang, K. Chang, Q. Yang, and W. Wu, "Semiconductor-Based Surface-Enhanced Raman Scattering Sensing Platforms: State of the Art, Applications and Prospects in Food Safety," *Trends in Food Science & Technology* 147 (2024): 104460.

35. Y. Xie, C. Chen, C. Zhang, et al., "Synergistic Enhancement of Ultrahigh SERS Activity via Cu_2O@Ag Core-Shell Structure for Accurate Label-Free Identification of Breast Tumor Subtypes," *Nano Today* 54 (2024): 102140, https://doi.org/10.1016/j.nantod.2023.102140.

36. C. Zhang, J. Tan, B. Du, et al., "Reversible Thermoelectric Regulation of Electromagnetic and Chemical Enhancement for Rapid SERS Detection," *Acs Applied Materials & Interfaces* 16 (2024): 12085–12094, https://doi.org/10.1021/acsami.3c18409.

37. X. Zheng, Z. Ye, Z. Akmal, C. He, J. Zhang, and L. Wang, "Recent Progress in SERS Monitoring of Photocatalytic Reactions," *Chemical Society Reviews* 53 (2024): 133868.

38. H. Zhou, J. Qiu, Y. Zhang, Y. Liang, L. Han, and Y. Zhang, "Self-Assembled C-Ag Hybrid Nanoparticle on Nanoporous GaN Enabled Ultra-High Enhancement Factor SERS Sensor for Sensitive Thiram Detection," *Journal of Hazardous Materials* 469 (2024): 133868, https://doi.org/10.1016/j.jhazmat.2024.133868.

39. E.-J. Zhang, T.-S. Deng, Y.-C. Cheng, et al., "Gold Nanobipyramids Coated With Silver–Platinum Alloy Shells for Plasmonically Enhanced Photocatalytic Degradation of Methyl Orange," *ACS Applied Nano Materials* 7 (2024): 14596–14608, https://doi.org/10.1021/acsanm.4c02124.

40. A. Dong, J. Chen, P. M. Vora, J. M. Kikkawa, and C. B. Murray, "Binary Nanocrystal Superlattice Membranes Self-Assembled At The Liquid–Air Interface," *Nature* 466 (2010): 474–477, https://doi.org/10.1038/nature09188.

Supporting Information

Additional supporting information can be found online in the Supporting Information section.

Supporting File: ppsc70108-sup-0001-SuppMat.docx.

Highly Uniform SERS Substrates Based on Ligand Concentration-Gradient Modulated Gold Nanobipyramid Self-Assembled Monolayers

Kun-Peng Wang[1], Jie Liu[1,], Xiaoyu Zhao[2], Zhigang Zhou[1], Tian-Song Deng[1,*]*

[*]Corresponding author. E-mail: dengts@pku.edu.cn; liujie4209@hdu.edu.cn

[1]School of Electronics and Information Engineering, Hangzhou Dianzi University, Hangzhou 310018, P. R. China.

[2]College of Materials and Environmental Engineering, Hangzhou Dianzi University, Hangzhou, P. R. China

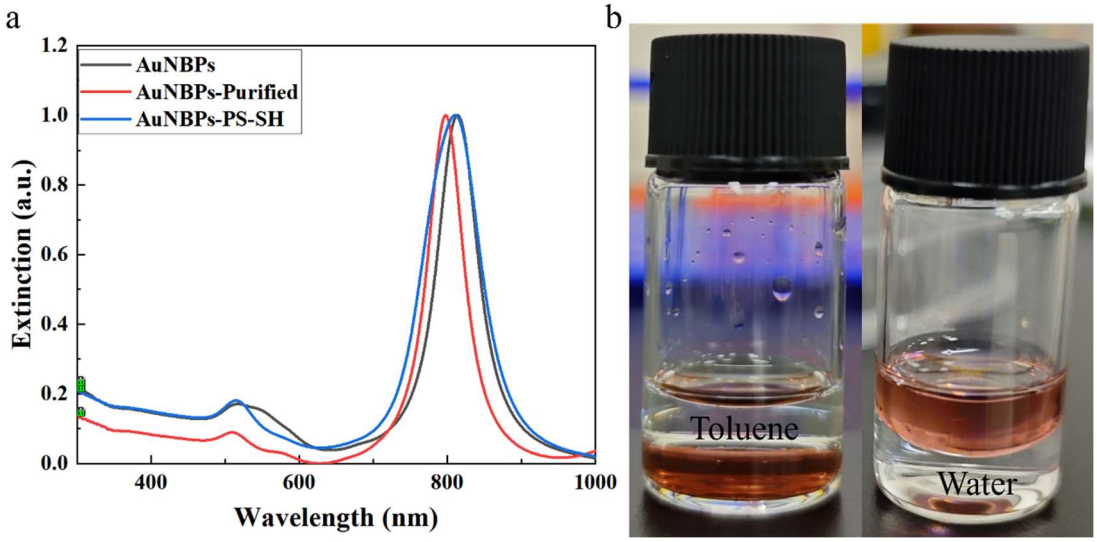

Figure S1. Surface modification and phase transfer of AuNBPs. (a) Extinction spectra of as-synthesized (black), purified (red), and AuNBPs-PS-SH (blue). (b) Photographic comparison of AuNBPs-CTAB aqueous solution (left) and AuNBPs-PS-SH toluene solution (right). After surface modification, the AuNBPs-PS-SH can be dispersed well in toluene.

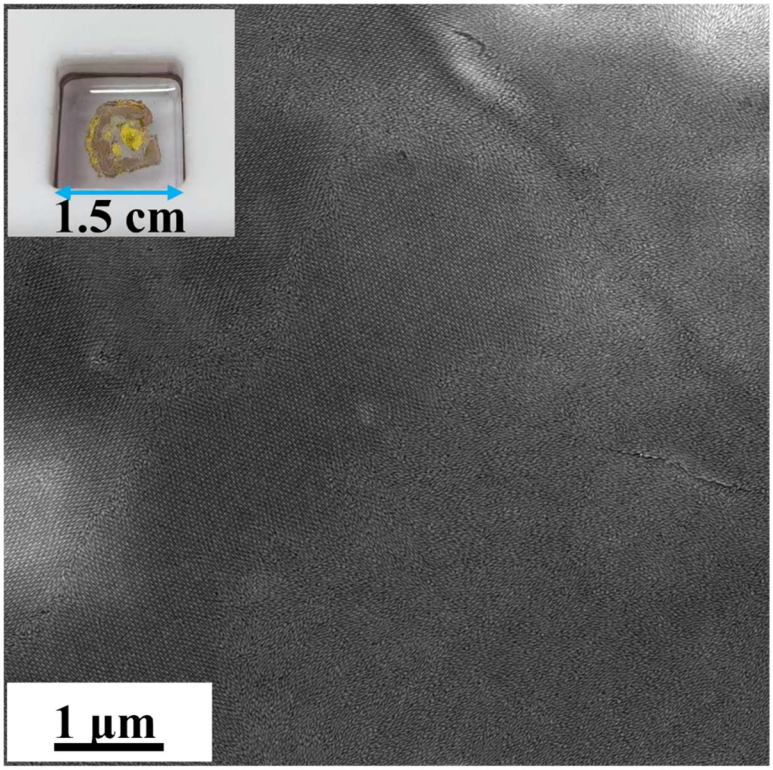

Figure S2. Low-magnification SEM image of the self-assembled monolayer formed from AuNBPs-PS-SH. Inset: a photograph of the AuNBPs film on DEG.

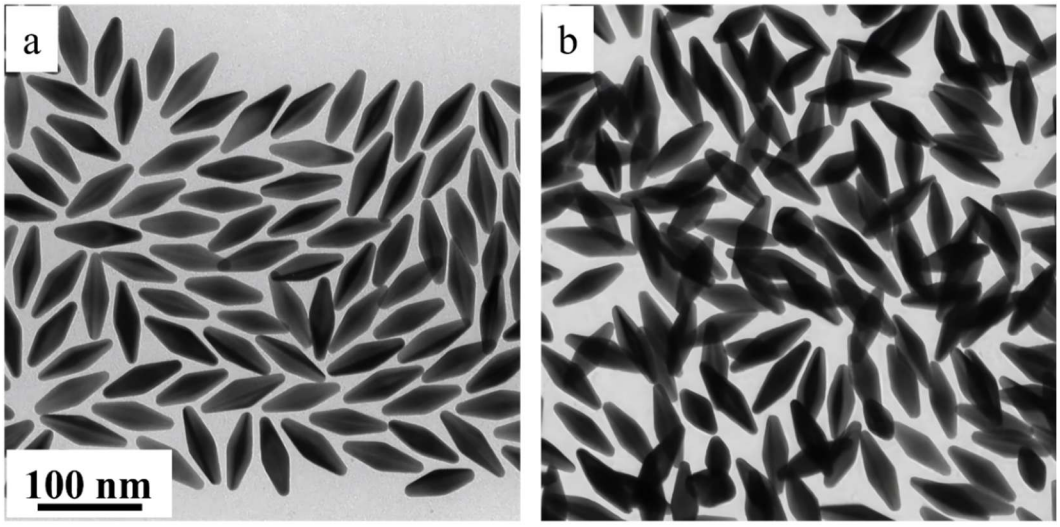

Figure S3. TEM images of monolayers self-assembled with different concentrations of free PS-SH (a) 2 mg/mL (b) 4 mg/mL. When the free PS-SH concentration exceeds the critical threshold (>1.2 mg/mL), the AuNBPs monolayer structure undergoes a distinct structural transition: at 2 mg/mL, the particles lose their parallel row alignment and adopt a disordered arrangement with significantly increased spacing; at 4 mg/mL, disordered multilayered aggregates are formed, leading to the complete collapse of the monolayer architecture.

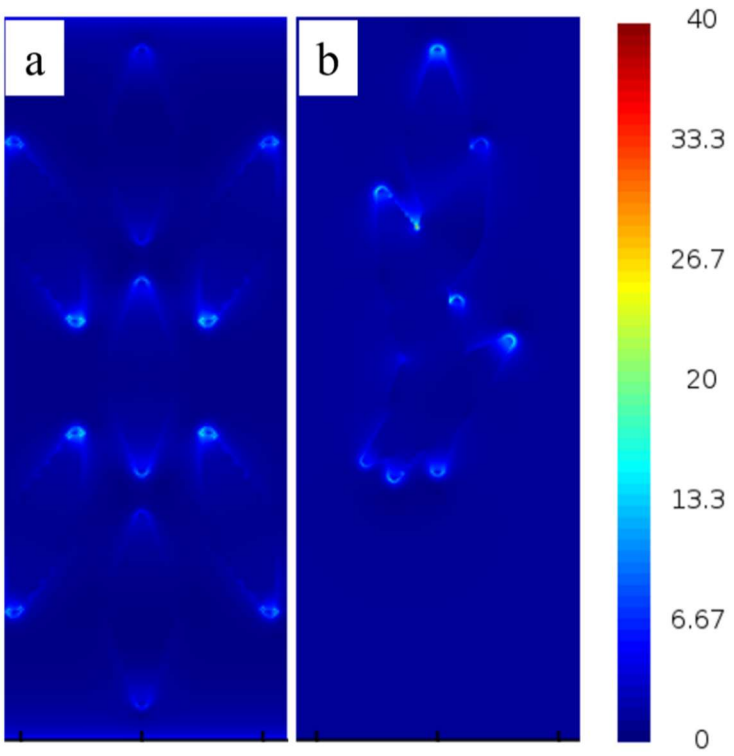

Figure S4. Finite-Difference Time-Domain (FDTD) simulations of electric field intensity distributions for AuNBPs monolayers self-assembled with free PS-SH concentrations of (a) 2 mg/mL, and (b) 4 mg/mL. Simulations in Figure S4 reveal that the disordered structures induced by excess free PS-SH (2 mg/mL and 4 mg/mL) lead to a significant attenuation of the electric field intensity to approximately 12 and 8, respectively. This result aligns perfectly with experimental observations, confirming that excessively high ligand concentrations weaken SERS performance due to structural disorder.